Sweep Frequency Response Analysis to Monitor and Identify Changes in the Impedance of a Photovoltaic Panel Measured Online using a Power Optimizer

Jeet Panchal
Center for Power Electronics Systems (CPES)
Virginia Polytechnic Institute and State University
Blacksburg, USA
jeetbp@vt.edu

Bo Wen
Milan Power Electronics Laboratory (MPEL)
Delta Electronics (Americas) Ltd
Durham, North Carolina, USA
wenbo@vt.edu

Rolando Burgos
Center for Power Electronics Systems (CPES)
Virginia Polytechnic Institute and StateUniversity
Blacksburg, USA
rolando@vt.edu

***Abstract*— Photovoltaic (PV) cells generally consist of a current source due to photocurrent, p-n junction diodes with parasitic resistance, capacitance, and inductance. This paper proposes online sweep frequency response analysis (SFRA) to measure the AC impedance of a PV panel using an existing panel-level power optimizer in a PV system. The algorithm will actively perturb a small signal into a 300 W rooftop PV panel and compute its small signal impedance. The technology discussed is easy to incorporate, requires no additional hardware, doesn't alter the stability of the system, and is implemented at a steady state point. The power optimizer initially stabilizes at an operating point and then perturbs the PV current via SFRA and computes PV panel ac impedance. The relative standard deviation test conducted indoors under 300 W/m^2 illumination on a PV panel shows less than 5% error in PV panel impedance magnitude and phase measured using a power optimizer.**

Keywords— Photovoltaics panel, AC impedance, small signal, SFRA, hot spot fault, short circuit fault, junction box fault

I. INTRODUCTION

The photovoltaic panel has been installed widely across the globe. According to National Renewable Energy Laboratory (NREL) analysis [1-2], 8 billion square meters of rooftops in the United States have the potential to install solar panels representing 1 terawatt of power. With large-scale PV installations, and upgrades in software algorithms in research. The health monitoring and fault estimation of the PV panel can be monitored by the power converter. [3-7] talks about AC impedance measurement of PV panels and highlights hot-spot detection of PV panels using AC impedance.

The AC impedance method is utilized in research to evaluate electrochemical device characteristics. Online impedance measurement is a helpful tool in the control system; the power converter can measure the input or output impedance in real time to monitor the stability and take corrective action if needed. Digital control with a modified correlation method as discussed in [8-11] is a helpful tool for power converter system identification to determine control-to-output response by cross-correlation of an input signal and sensed output signal. Using multi-period pseudo-random binary signal (PRBS) injection to the control input, input and output impedance is measured as shown in [12-15]. The online AC impedance technique is utilized in the power converter to measure PV panel ac impedance using a PRBS. Fault monitoring and detection can eventually decrease the operational and maintenance cost of a PV system. [16] The report mentioned the mathematical derivation and the software-based model to estimate the operational and maintenance cost related to photovoltaic systems. The cost model takes a few assumptions on system size, type, environmental conditions, and age to provide a detailed cost change over a very long performance period.

Using an online technique such as mentioned in [8-12], a power converter can inject multi-tone in the system can measure the AC impedance of the PV panel. But, with a low pass filter present at the voltage and current sensor in the existing PV panel, the measured impedance will be attenuated [18]. Single-tone small signal injection injects and computes single frequency response at a time and decreases the relative deviation of measurement. This increases the effectiveness of the PV panel AC impedance measured. This paper is organized as follows: Section II describes the small signal impedance of the PV panel and measurement results using an offline technique. An SFRA-based online impedance measurement technique using a power optimizer is discussed in section III. Section IV presents indoor and outdoor online measurements of PV panel impedance using the proposed technique. The conclusions are drawn in section V.

II. PV PANEL IMPEDANCE

A. Small Signal Impedance

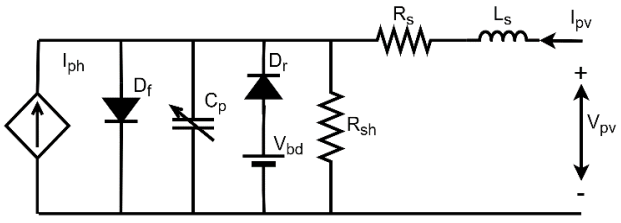

Figure 1 Dynamic PV cell equivalent circuit

A PV cell is part of a PV panel connected in series or parallel combination among multiple PV cells. A PV cell under specific illumination and temperature produces voltage and current [17]. The illumination (G) and temperature (T) of the PV panel affect the photocurrent (I_{ph}), forward diode (D_f), reverse diode (D_r), parallel capacitance (C_p), shunt resistance (R_{sh}), and breakdown voltage (V_{bd}) as shown in Figure 1Figure 1 to determine the voltage and current of the PV

panel. The equations given in [] help in analytically deriving the panel voltage as shown in (1) based upon illumination, temperature, and panel current where PV panel current (I_{PV}), diode voltage ($V_{d,}$) are depended on G and T, and series resistance (R_s) and series inductor (L_s) are fixed.

$$V_{pv}(V_d, I_{pv}) = V_d - I_{pv}R_s - L_s\frac{dI_{pv}}{dt} \quad (1)$$

The series resistance and inductor of a PV panel are dependent on the parasitic involved in the manufacturing of the PV panel and thus maximum power point (MPP) in the current- voltage (I-V) characteristics of a PV panel varies under increase or decrease of series resistance. Applying a small signal to the dynamic model shown in Figure 1, the effects of I_{ph}, D_f, D_r, $R_{s,h}$ and V_{bd} are cumulatively considered to be parallel resistance (Rp) and C_p. The small signal impedance of the PV panel (Z_{PV}) is analytically derived as (2)

$$Z = \left(R_p \parallel {}^{1}/_{sC_p}\right) + R_s + sL_s \quad (2)$$

Table 1 Parameters for 300 W PV panel

Condition	R_s (Ω)	R_p (Ω)	C_p (μF)
Normal	0.046	0.0352	185
R_p ↑	0.046	0.352	185
C_p ↑	0.046	0.0352	1850

Equation 2 shows the dependency of R_p and C_p on Z_{PV}, also from above G, and T vary the operating point I_{PV} and V_{PV}. Thus, with variation in G and T, Z_{PV} also varies. Using the bode plot, the impedance magnitude and phase for the PV panel under three different conditions as shown in Table 1 are plotted and shown in Figure 2. Under normal conditions, for

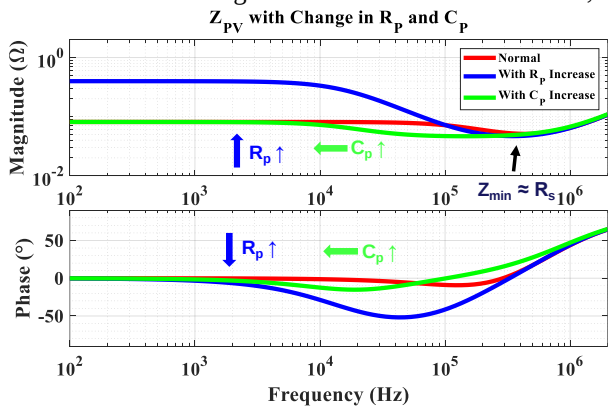

Figure 2 Z_{PV} based upon equation (2) and using data from Table 1

low frequency range the behavior of Z_{PV} is resistive with a magnitude equal to the sum of R_s and R_p, under medium frequency range the effect of C_p and R_P dominants with decreasing the magnitude and phase of Z_{PV}, under high frequency range the effect of series inductor dominates with increase magnitude and phase of Z_{PV}. Under resonant frequency due to L_s and C_p, the minimum magnitude of Z_{PV} will be R_s of the PV panel. With increasing the R_p as in condition 2, the magnitude of Z_{PV} increases under the low-frequency range and phase decreases under the medium frequency range. With increasing C_p under condition 2, the effect of C_p in the Z_{PV} becomes more prominent at a lesser frequency under medium frequency range as compared to normal conditions thus bode plot is noticed shifting left.

B. *Offline Z_{PV} Measurement*

a) Solar Simulator

a Front view *b Side view*

Figure 3 Solar simulator for illuminating 300 W PV panel

From above, the Z_{PV} is dependent on G and T, thus a solar simulator as shown in Figure 3 is built in CPES Laboratory to real-time measure Z_{PV}. The solar simulator consists of a 300 W rooftop PV panel from Grape Solar Ltd. with 60 monocrystalline PV cells connected in series. The maximum power of a PV panel under 1000 W/m^2 illumination and 25 °C temperature is 300 W, with an MPP voltage of 32.48 V and MPP current of 9.24 A. The junction box of the PV panel has 3 bypass diodes with each diode connected in parallel to 20 PV cells. The PV panel in the solar simulator is illuminated using LED sheets, providing in total of 300 W/m^2 illumination to the PV panel. Thus, the power source by PV panel in the solar simulator at 300 W/m^2 under MPP is 75 W with an MPP voltage of 35 V and MPP current of 2.14 A.

b) Signal Injection for Offline Z_{PV} Measurement

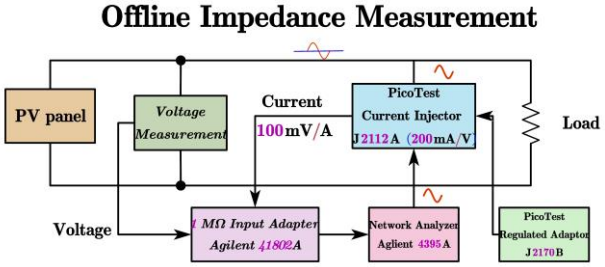

Figure 4 Offline AC impedance measurement of PV panel using current injection

The impedance of the illuminated PV panel in the solar simulator is measured using a PicoTest current injector J2112A as shown in Figure 4. The PV panel impedance is measured at the operating point determined by the external load connected to the PV panel. The small signal perturbation is injected through the current injector which acts as a voltage-controlled current source with a gain of 0.2 V/A. The network analyzer Agilent 4395 A injects signal in the current injector with 0 dBm power, sweeping 201 data points and bandwidth 100 Hz to 200 kHz. Network Analyzer measures impedance magnitude and phase using sensed AC from the current injector and voltage across the PV panel via 1 MΩ input adapter Agilent 41802A. MATLAB is used to calculate Z_{PV} from impedance measured using a network analyzer.

c) Offline Z_{PV} Measurement under PV Panel Fault

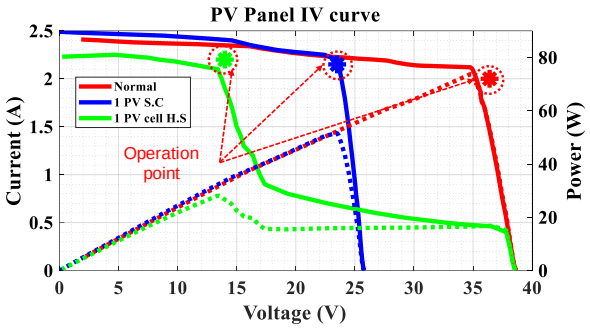

a PV panel I-V and P-V characteristics

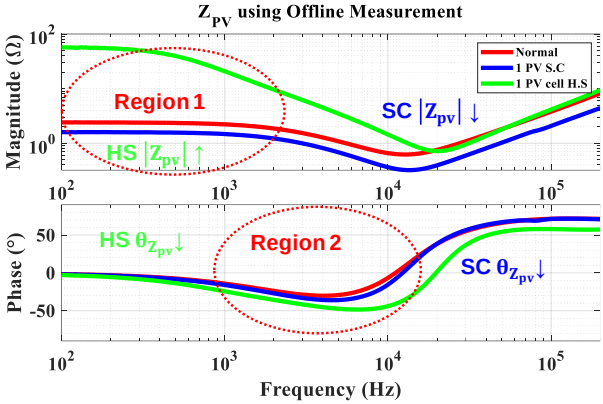

b PV panel Z_{PV} at operating points marked above

Figure 5 Offline Z_{PV} measurement

The PV panel under normal conditions with the illumination of 300 W/m^2 in solar simulator I-V and P-V characteristics is measured using BK precision 8500 electronic loads. The electronic load input current is varied and PV panel voltage and current are noted to obtain PV panel I-V (solid line) and P-V (dashed line) characteristics as shown in Figure 5. Two different fault situations are demonstrated to compare the behavior of PV panel I-V, P-V characteristics, and Z_{PV} from the normal condition. First, a short circuit (S.C.) fault situation is performed by short-circuiting one of three bypass diodes in the junction box of the PV panel. Thus, only 40 PV cells as shown in Figure 6 will source power under 300 W/m2 illumination and PV panel I-V and P-V characteristics are measured and shown in Figure 5 from the above-mentioned procedure. Lastly, a single PV cell hot spot (H.S) fault is demonstrated where a bypass diode from three bypass diodes is open-circuited in the junction box and 1 PV cell of 20 PV cells whose bypass diode is open-circuited is covered so as the illumination on that PV cell is 0 W/m2. Thus, 59 PV cells are illuminated at 300 W/m2 and the PV panel has 2 bypass diodes active as shown in Figure 6, PV panel I-V and P-V characteristics are measured and shown in Figure 5.

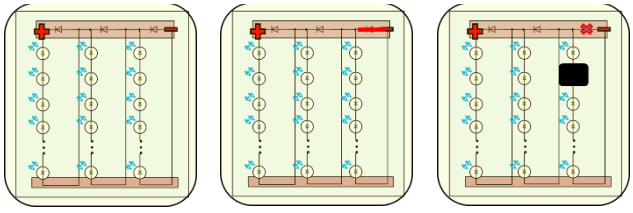

a Healthy *b S.C fault* *c H.S fault*

Figure 6 PV panel conditions under test

Comparing PV panel, I-V characteristics from Figure 5, under PV panel S.C fault condition only 40 PV cells are sourcing power to the load thus the voltage will be 2/3rd of the voltage under normal conditions for current less than MPP. Under PV panel H.S fault condition, the covered/shaded PV cell goes in the reversed biased state, thus the voltage across the shaded PV cell is negative also the open-circuited bypass diode allows the voltage to go negative. With shaded PV cell negative voltage and PV cell sourcing current, the cumulative effect will be shaded PV cell sinking power, and thus the temperature of the PV cell increases. The temperature of the shaded PV cell measured using the FLIR E5 thermal imager went up to 110 °C under 30 minutes of operation. Comparing the PV panel, I-V characteristics of the H.S fault with the normal condition, the shaded PV cell tends to decrease the power of the PV panel with reverse biased voltage, thus the overall PV panel voltage decreases under MPP.

PV panel small signal impedance is measured at the operating point marked in I-V characteristics for normal conditions using the procedure as discussed above. The Z_{PV} magnitude and phase are shown in Figure 5, considering three frequency zone: low, medium, and high. Comparing the analytical results from above with the offline measured Z_{PV} under normal conditions, under a low-frequency range both the results show resistive behavior as discussed above. Under the medium frequency range, the capacitive behavior of C_p is noticed, and inductive behavior dominates under the high-frequency range. Thus, the behavior of Z_{PV} can be compared to the analytical equation (2).

Under PV panel S.C fault condition, Z_{PV} is measured at the operating point marked in the I-V characteristics for S.C fault condition. Comparing Z_{PV} of normal condition with 1 PV string S.C condition, due to short circuit action, the $|Z_{PV}|$ decreases in all three-frequency ranges. Also, a slight change in the phase of Z_{PV} is noticed due to a change in C_p due to short circuit conditions.

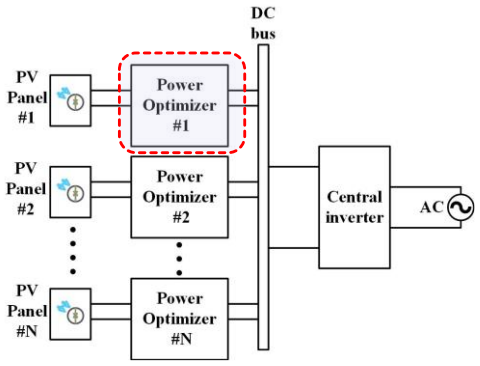

Figure 7 PV panel power extraction using power optimizer

Under the PV panel, 1 PV cell H.S fault condition, Z_{PV} is measured at the operating point marked in the I-V characteristics for the H.S fault condition. Comparing small signal Z_{PV} H.S fault with normal conditions, as mentioned in [5], under the H.S condition, the shaded PV cell gets reverse biased. Also under reverse bias conditions, the diffusion capacitance effect dominates overall capacitance in C_p. The PV cell reverse characteristics lie under constant current region which tends to increase the R_p of the shaded PV cell thus, increases the overall $|Z_{PV}|$ of the PV panel. From above with an increase in Rp and Cp, the effects seen in Figure 2 such as an increase in $|Z_{PV}|$ under low-frequency range, earlier

dominance of C_p in medium frequency range can be seen in small signal Z_{PV} of 1 PV cell H.S fault condition as well.

III. SFRA Implementation in Power Optimizer (P.O)

The offline technique for Z_{PV} measured using small signal injection involved a solar simulator with a 300 W PV panel, and experimental equipment such as a signal injector, resistive load for sinking power, and network analyzer to measure Z_{PV}. Considering residential rooftops as shown in Figure 7, where the PV panel sources power to the AC grid through power optimizer and central inverter. The PV panel is operated under MPP using power optimizer. The power optimizer has all the necessary tools for measuring Z_{PV} such as a switch to inject small signal perturbation, voltage and current sensor for measurement, and, DSP for computation.

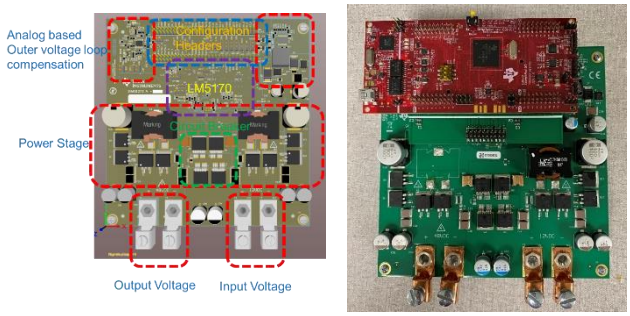

a P.O peripheral details *b P.O with MCU*

Figure 8 P.O used for online Z_{PV} measurement

Commercially available power optimizer follows standards for the waterproofing power optimizer and thus accessing the control stage becomes difficult. Texas Instrument LM5170EVM as shown in Figure 8 is a DC/DC buck-boost converter for battery charging applications. The LM5170EVM has an input voltage range from 3 V to 48 V and an output voltage range from 6 V to 75 V with maximum power up to 300 W. The PV panel I-V characteristics under different conditions such as normal, 1 PV cell H.S fault, 1 PV string S.C fault as shown in Figure 5, has wide input range. Thus, the specification is suitable for operating an evaluation board as a power optimizer. The DC/DC converter is modified in the section below for the power optimizer application.

A. Power Converter Modifications

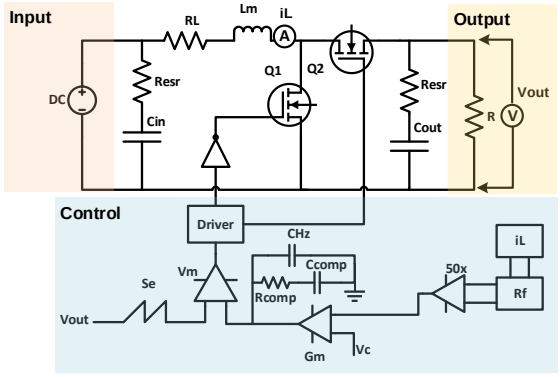

Figure 9 P.O circuit diagram with the average current control mode

Referring to Figure 7, the multiple P.O is connected to the DC bus to source power to gird. To reduce the conduction loss, the P.O. are generally operated in boost mode. Thus, the evaluation board is modified to DC/DC boost converter mode as shown in the Figure 9. The inductor current in the evaluation board power stage is controlled using average current mode control as shown in Figure 9. An interface board with Texas Instrument launchpad – 28379D is connected to configuration header pins for externally commanding operations such as converter ON/OFF, boost mode, measured voltage and current sensor analog data and setting current reference for current control mode.

a) Modifying DC/DC Converter Power Stage

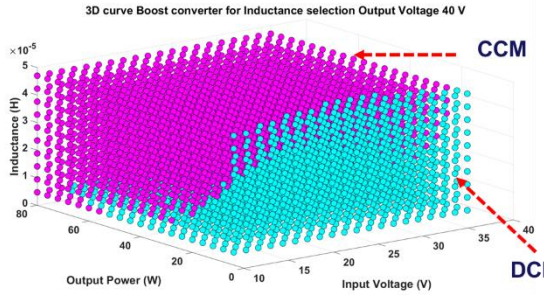

Figure 10 3D curve for CCM and DCM mode comparison with the varying input voltage, output power, and inductance

Under PV panel fault conditions such as H.S. fault or S.C fault, the PV panel enters light load, under these conditions the PV panel should operate under Continuous conduction mode (CCM). Figure 10 shows conditions for CCM and compares discontinuous conduction mode (DCM) operation with sweeping inductor along with input voltage and output power based upon equation 3.

$$\frac{V_{in}}{\acute{D}^2 R} > \frac{DT_s V_{in}}{2L} \quad for\ CCM \tag{3}$$

Also, under low inductance the inductor current ripple increases based on equation 4.

$$Inductor\ ripple\ current = \frac{V_{in} D}{2F_{sw} L} \tag{4}$$

Using equation 4, Figure 11 shows the variation of the inductor current ripple with sweeping inductance, switching frequency, and input voltage under 40 V output voltage.

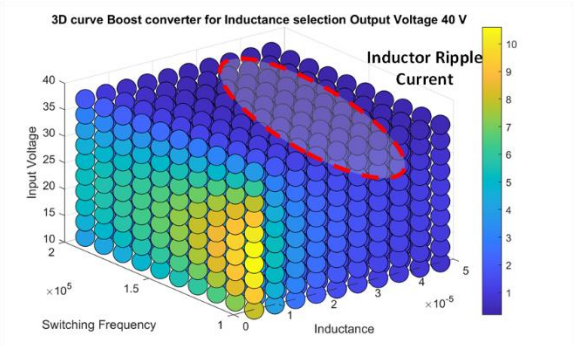

Figure 11 P.O inductor ripple current under varying inductance, switching frequency, and input voltage

From Figure 10 and Figure 11, the higher switching frequency will account to lower inductor ripple, and CCM operation is attained with higher inductance. With higher switching frequency and inductance, losses in the system will increase.

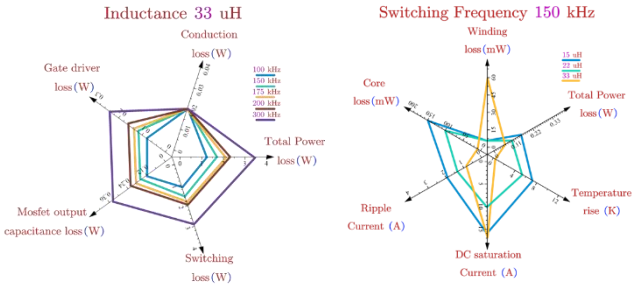

a MOSFET loss comparison *b Inductor loss comparison*

Figure 12 P.O power stage loss comparison

Figure 12, shows a comparison of losses using an analytical equation from [] in a converter under increasing switching frequency with 33 µH inductance. Also, the above-mentioned figure shows inductor losses computed using REDEXPERT WÜRTH ELEKTRONIK [] software based upon inductance available by Würth Elektronik with similar dimension. Based upon above analysis 150 kHz switching frequency and 33 µH inductance is selected for the power stage.

b) Modifying DC/DC Converter Control Stage

The power stage is optimized for CCM operation under light load conditions as discussed above. Further, the G_{id} plant model as shown in equation 5 alters due to modifications in power stage where R_f is sensor gain, G_m is transconductance gain, G_{comp} is compensator gain, and V_m is modulator gain.

$$G_{id} = \frac{2V}{\acute{D}^2 R}\left(\frac{1+s\frac{RC}{2}}{1+s\frac{L}{\acute{D}^2 R}+s^2\frac{LC}{\acute{D}^2}}\right) \quad 5$$

Using Gid, loop gain of the system is analytical computed and a type 2 compensator as shown in equation 6 is designed to achieve higher bandwidth and higher phase margin for stable operation. The updated RC network in evaluation board are R_{comp} 25 kΩ, C_{comp} 1 nF, C_{HZ} 100 pF. The system model is simulated in SIMPLIS software, and the inductor current closed loop gain is computed analytically to compared with SIMPLIS as shown in Figure 13.

$$G_{comp} = \frac{1}{C_{comp}}\left(\frac{1+sR_{comp}C_{comp}}{s\left(1+sR_{comp}C_{HZ}\right)}\right) \quad 6$$

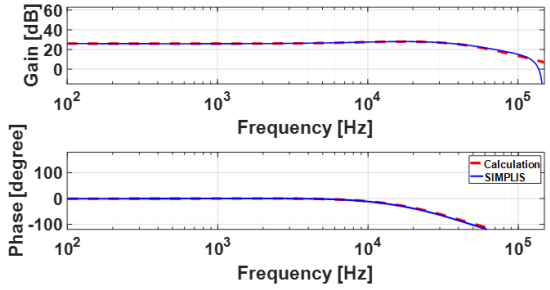

Figure 13 Inner current control to output gain bode plot

The above-mentioned figure shows the closed loop bandwidth around 22 kHz which is 1/7th of the switching frequency of the switches in the power stage. Thus, the small signal frequency to measure Z_{PV} using a power optimizer must be less than the bandwidth of the closed loop gain. The evaluation board has a current sensor to measure inductor current and voltage sensors to measure input and output voltages. The low pass filters for sensors present in the system are 20kHz for current sensor and 300 Hz for input and output voltage. Thus, based upon inductor current closed loop gain bandwidth and sensors low pass filter bandwidth, the small signal injection bandwidth in P.O. from 10 Hz to 1000 Hz range.

B. SFRA Based Small Signal Implementation in P.O.

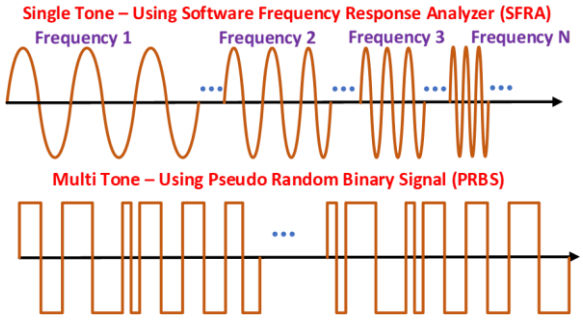

Figure 14 Types of small signal injection

The microcontroller unit (MCU) launch pad -28379D provides a reference control signal to P.O. based upon sensed voltage and current at the input and output end. For small signal impedance measurement, the small signal perturbs above the reference signal which is given to the P.O., further the compensator compares the reference with the inductor current and varies the duty cycle to inject perturbation in inductor current of the P.O. The Figure 14 shows the comparison of single tone perturbation with a multi-tone.

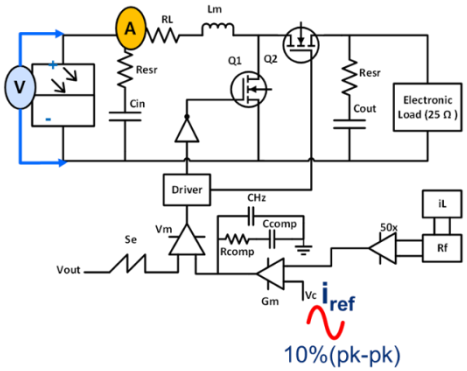

Figure 15 Small signal injection via SFRA

A single-tone small signal injects sweeps multiple pulses of a single frequency at a time compared to a multi-tone small signal injects a band of frequency all together. This increases the computation time for single-tone signal, either to compute one frequency at a time, whereas multi-tone stores the real-time data of small signals and later analysis the response. This leads to an increase in memory storage for multi-tone signal injections as compared to signal-tone injections. Also, single-tone small signal sweep takes a longer time due to single frequency injection, whereas multi-tone sweep is quicker. For online power converter-based implementation, Texas Instruments-based software frequency response analyzer (SFRA) is a C-based code for single-tone small signal injection implementation. Multi-tone signals use a pseudo-binary random signal (PRBS) generator for generating signal which can be generated using a Simulink-based embedded code generator. Due to memory shortage, Single-tone online

impedance measurement is implemented to measure Z_{PV} and compare Z_{PV} under normal and faulty conditions.

TI-based sweep frequency response analyzer (SFRA) is used to generate a small signal in the reference signal provided to the P.O. to inject a small signal into the inductor current as shown in Figure 15. SFRA injects a small signal from 10 Hz to 1 kHz, with 100 frequency points and the measurement time is 1 minute per response. Figure 16 shows the procedure to measure Z_{PV} using SFRA based small signal injection in P.O. The small signal amplitude is 10% of the reference signal, the PV panel operates at or near the MPP and the operation is stable. Further, PV panel impedance is computed utilizing two different responses via SFRA. Initially, control to inductor current response (vc-iL) is measured, and later control to input voltage (vc-Vin) response is measured. Dividing the above-mentioned two responses gives the input impedance (Zin) of the power converter. The Zin consists of input capacitance impedance (Zc) and ZPV under the operating conditions, MATLAB is used to analytically compute PV panel impedance (Zpv) using equation 6.

$$Z_{pv} = \left(\frac{1}{Z_{in}} - \frac{1}{Z_c}\right)^{-1} \qquad 6$$

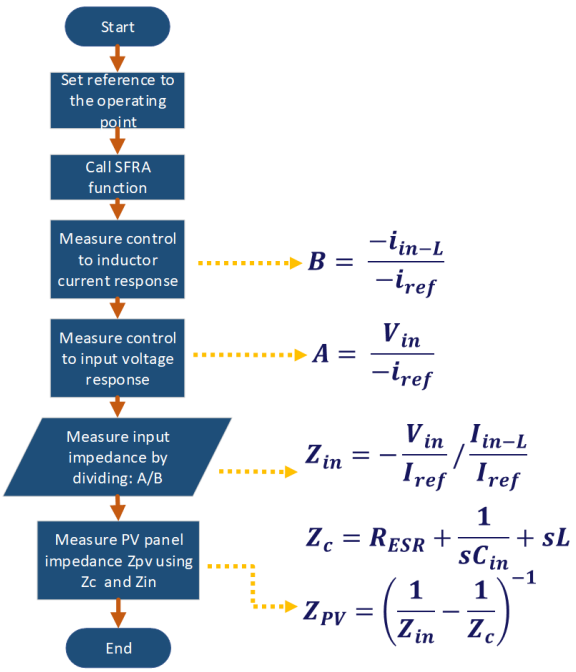

Figure 16 Flowchart to compute PV panel impedance using SFRA

IV. Z_{PV} Measurement using SFRA Technique

A. Indoor Z_{PV} Measurement

The solar simulator illuminates the PV panel under 300 W/m^2 illumination and steady temperature, the PV panel is connected to the input of the P.O., and the output of the P.O. is connected to the BK Precision 8500 electronic load. The electronic load is operating under constant power load as shown in Figure 15. Online PV panel Z_{PV} measurement is implemented using SFRA also three different conditions are compared as stated in Figure 6.

Figure 17 shows the comparison of I-V and P-V characteristics of PV panels under normal conditions, 1 PV string S.C fault condition, and 1 PV cell H.S fault condition. The I-V and P-V characteristics for all three cases measured during offline measurement as shown in Figure 5 and online measurement shows similarities, but the operational points are slightly drifted in offline measurement due to temperature fluctuation in the solar simulator.

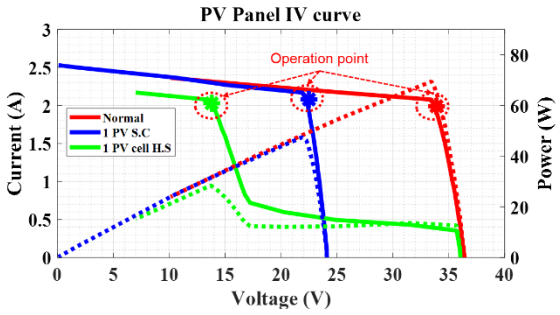

a PV panel I-V and P-V characteristics

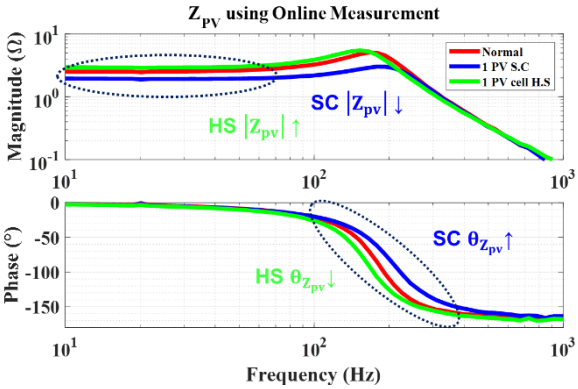

b PV panel Z_{PV} at operating points marked above

Figure 17 Indoor Online Z_{PV} measurement

The P.O. injects a small signal to the operational points marked on the I-V characteristics as shown in Figure 17. The computed PV panel Z_{PV} measured using the flowchart in Figure 16 for all three cases is compared and shown in Figure 17. Under the low-frequency region as marked in the above-mentioned figure, the $|Z_{PV}|$ for 1 PV cell H.S fault condition is higher than the normal condition and is lower for 1 PV string S.C fault condition. As discussed above, the R_p increases during PV cell reverse biased condition which tends to increase $|Z_{PV}|$ for H.S fault condition. Also, R_s and R_p decreases due to short-circuiting condition thus overall |ZPV| decreases in S.C fault condition. Under the medium frequency range as marked in the above-mentioned figure, the H.S. fault shows earlier phase dropping of Z_{PV} as compared to the normal condition due to an increase of Cp under reverse biased condition. Also, the C_p decreases as compared to normal under short-circuit conditions in 1 PV string S.C fault, thus the Z_{PV} phase is higher in PV panel S.C fault as compared to normal conditions. The online PV panel Z_{PV} trend in magnitude and phase shows similarities with offline measurement when H.S. and S.C. fault conditions are compared to normal conditions.

The online PV panel $|Z_{PV}|$ is further extended to measure a junction box (J.B) fault in the PV panel. Due to corrosion or improper soldering [8] of contact leads in the PV panel, the contact resistance increases, and with time and an increase in temperature this increase in resistance can cause a junction box fault. A series resistance of 0.1 Ω is added to the junction box to demonstrate a junction box fault.

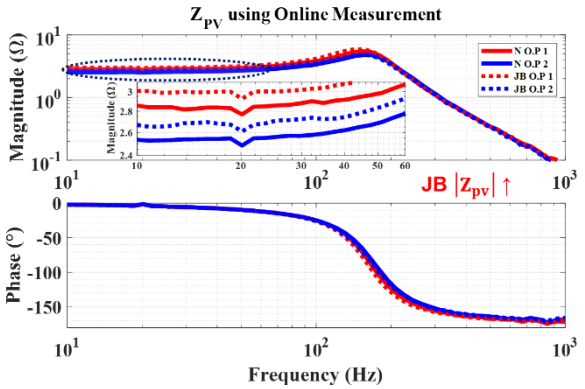

a

Figure 18 Junction box fault Z_{PV} measurement

Figure 18 shows the I-V and P-V characteristics of a PV panel under normal conditions, also due to a slight change in the resistance, the effective PV panel I-V and P-V characteristics are not much affected. The PV panel Z_{PV} curve comparison is shown in Figure 18. The increase in the $|Z_{PV}|$ under the low-frequency range for the impedance at the operating points marked is 0.14 Ω due to additional external resistance connected to the PV panel. Thus, SFRA-based online PV panel Z_{PV} is useful to detect junction box faults of PV panels.

B. *Outdoor Z_{PV} Measurement*

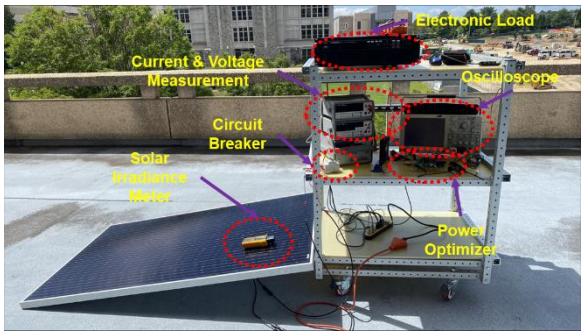

Figure 19 Hardware setup for outdoor AC impedance measurement of PV panel

The results shown above sections are using a solar simulator with 300 W/m2 illumination sourcing 75 W PV panel power under MPP. The online PV panel impedance measurement is further conducted outdoors on the third-floor balcony of Whittemore Hall under Sun's illumination as shown in Figure 19. On a bright sunny day, the illumination on the PV panel varies with peak illumination around 1000 W/m2, under this illumination PV panel sources 300 W to power the optimizer. Further, the P.O. is connected to BK precision 8610 electronic load to sink the power, the sun's irradiance is measured using Fluke IRR1-SOL solar irradiance meter. Tektronix TDP1500 differential probe and Tektronix TCP0020 current probe is used to observe PV panel voltage and current on a mixed signal oscilloscope Tektronix MSO5104.

Figure 20, shows the comparison of PV panel I-V and P-V characteristics under 920 W/m2 illumination for normal conditions and S.C fault conditions. PV panel impedance is measured at the operating points marked on the I-V characteristics for both conditions. Figure 20, shows the PV panel impedance for both conditions. Under the low-frequency range, a decrease in $|Z_{PV}|$ and an increase in the PV panel impedance phase is due to the S.C condition for the PV panel. The results show similarity with indoor measurement results as discussed above. Thus, P.O. based online PV panel impedance measurement technique is useful to characterize faults based on comparing the impedance with normal.

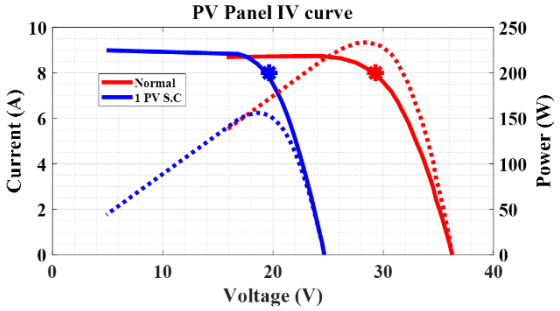

a PV panel I-V and P-V characteristics

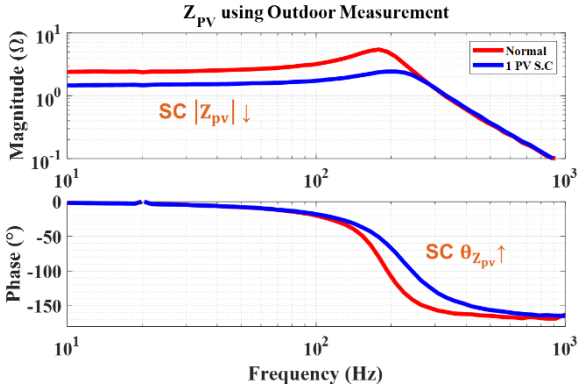

b PV panel Z_{PV} at operating points marked above

Figure 20 Outdoor online Z_{PV} measurement for S.C fault

C. *Relative Standard Deviation (R.S.D) for SFRA-based Z_{PV} Measurement*

The online impedance measurement is tested for relative standard deviation to understand the variation under PV panel faults at measured frequency points. Each PV fault impedance is measured 10 times at 100 different frequency points. Equation (7) calculates the relative standard deviation (R.S.D) of PV panel impedance under faulty conditions. Where xi is the mean of the sample data, x is the sample data, and N is the number of data points. The R.S.D of PV panel impedance test under fault conditions like hot spot fault, short circuit fault, and junction box fault is shown in Figure 21. For each PV panel fault, at all the measured frequency points, the R.S.D is less than 5 %. Thus, the effectiveness of the online impedance measurement is evaluated with less than 5 % error in the measured data.

$$R.S.D = \frac{\sqrt{\sum((x_i - x)^2)/N}}{x} \quad (7)$$

CONCLUSION

Under continuous operation of a PV panel for a longer time, it might undergo multiple faults such as hot spot fault, short circuit fault junction box fault as discussed. The power optimizer installed with each PV panel has a facility to real-time monitor the health of the PV panel. Online Impedance measurement technique as discussed in the paper utilizes voltage and current measurement data from the installed sensors in the P.O. and in real-time provides the change in the

PV panel impedance. TI-based boost converter with DSP is used to identify changes in the PV panel impedance based upon three different conditions such as healthy, hot spot fault, and short circuit fault in a PV panel. The paper measures PV panel impedance on a commercially available 300 W PV panel, also the PV panel is illuminated indoors using an in-house LED-based solar simulator and further tested outdoors under the sun's irradiance. The paper evaluates the effectiveness of the proposed technique by measuring the PV panel impedance multiple times to calculate the R.S.D under different conditions.

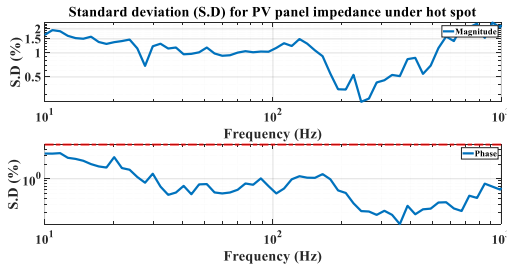

a H.S fault condition

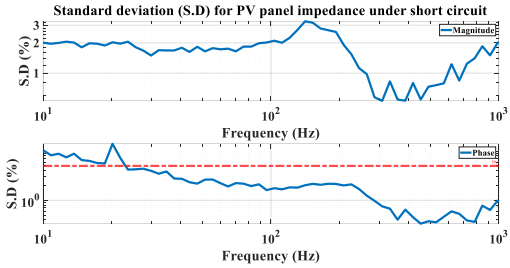

b S.C fault condition

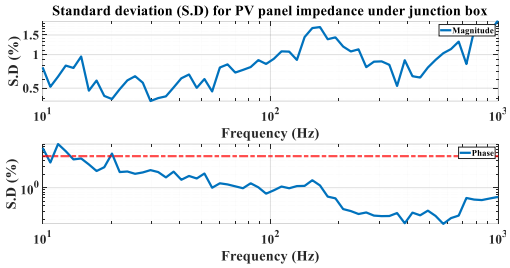

c J.B fault condition

Figure 21 R.S.D for computing effectiveness of online impedance measurement

The power converter bandwidth is low, less than 3 kHz; thus, the small signal response is limited to 2 kHz. A possible solution would be to increase the inner current control loop bandwidth to 1/5th of the switching frequency. The SFRA-based small signal injection takes 1 – 1.5 minutes for injection and computation; thus, the operation point can get shifted due to changes in irradiance, and the multi-tone small signal can be used for a fast response in the future. Signal conditioning is required for voltage, and current sensed after ADC due to the low pass filter present at ADC input, a high bandwidth filter can be used for noise attenuation.

ACKNOWLEGDEMENT

REFERENCES

[1] Wesley Cole, Daniel Greer, Jonathan Ho, Robert Margolis, “Considerations for maintaining resource adequacy of electricity systems with high penetrations of PV and storage”,Applied Energy,Volume 279,2020,115795,ISSN 0306-2619.

[2] Curtis, Taylor L., Heather Buchanan, Garvin Heath, Ligia Smith, and Stephanie Shaw. 2021. Solar Photovoltaic Module Recycling: A Survey of U.S. Policies and Initiatives. Golden, CO: National Renewable Energy Laboratory. NREL/TP-6A20-74124

[3] K. A. Kim, C. Xu, L. Jin, and P. T. Krein, “A Dynamic Photovoltaic Model Incorporating Capacitive and Reverse-Bias Characteristics,” IEEE J. Photovoltaics, vol. 3, no. 4, pp. 1334–1341, Oct. 2013, doi: 10.1109/JPHOTOV.2013.2276483.

[4] N. Akpolat, Y. Yang, F. Blaabjerg, E. Dursun, and A. E. Kuzucuoglu, “Modeling Photovoltaic String in PLECS Under Partial Shading,” in 2019 International Conference on Power Generation Systems and Renewable Energy Technologies (PGSRET), Istanbul, Turkey, Aug. 2019, pp. 1–6. doi: 10.1109/PGSRET.2019.8882698.

[5] C. Chamberlin, M. A. Rocheleau, M. W. Marshall, A. M. Reis, N. T. Coleman, and P. A. Lehman, “Comparison of PV module performance before and after 11 and 20 years of field exposure,” in Proc. IEEE Photovoltaic Specialists Conf., June 2011, pp. 101–105

[6] A. Mellit, G. M. Tina, and S. A. Kalogirou, “Fault detection and diagnosis methods for photovoltaic systems: A review,” Renewable and Sustainable Energy Reviews, vol. 91, pp. 1–17, Aug. 2018, doi: 10.1016/j.rser.2018.03.062.

[7] K. A. Kim, G.-S. Seo, B.-H. Cho, and P. T. Krein, “Photovoltaic Hot-Spot Detection for Solar Panel Substrings Using AC Parameter Characterization,” IEEE Trans. Power Electron., vol. 31, no. 2, pp. 1121–1130, Feb. 2016, doi: 10.1109/TPEL.2015.2417548.

[8] K.-M. Jakobi, W. Nasse, D. M. Parterna, D. F. Ansorge, C. Baar, and K. Ring, “FAULTS OF CONTACTS IN PV MODULE JUNCTION BOXES DUE TO FRETTING CORROSION,” p. 6.

[9] O. I. Olayiwola and P. S. Barendse, “Photovoltaic Cell/Module Equivalent Electric Circuit Modeling Using Impedance Spectroscopy,” IEEE Trans. on Ind. Applicat., vol. 56, no. 2, pp. 1690–1701, Mar. 2020, doi: 10.1109/TIA.2019.2958906.

[10] S. Osawa, T. Nakano, S. Matsumoto, N. Katayama, Y. Saka, and H. Sato, “Fault diagnosis of photovoltaic modules using AC impedance spectroscopy,” in 2016 IEEE International Conference on Renewable Energy Research and Applications (ICRERA), Birmingham, United Kingdom, Nov. 2016, pp. 210–215. doi: 10.1109/ICRERA.2016.7884539.

[11] T. Yokoi, K. Takechi, and H. Kakigano, “Impedance Measurement Method for Solar Cell Evaluation using a Power Converter,” in 2019 IEEE Third International Conference on DC Microgrids (ICDCM), Matsue, Japan, May 2019, pp. 1–6. doi: 10.1109/ICDCM45535.2019.9232790.

[12] S.-Y. Chiu, K. A. Kim, and Y.-C. Liu, “Analysis of Nanosatellite Impedance Interaction and Stability Based on System Operation Mode,” in 2021 IEEE International Future Energy Electronics Conference (IFEEC), Taipei, Taiwan, Nov. 2021, pp. 1–6. doi: 10.1109/IFEEC53238.2021.9662020.

[13] B. Miao, R. Zane, and D. Maksimovic, “System Identification of Power Converters With Digital Control Through Cross-Correlation Methods,” IEEE Trans. Power Electron., vol. 20, no. 5, pp. 1093–1099, Sep. 2005, doi: 10.1109/TPEL.2005.854035.

[14] A. Riccobono et al., “Stability of Shipboard DC Power Distribution: Online Impedance-Based Systems Methods,” IEEE Electrific. Mag., vol. 5, no. 3, pp. 55–67, Sep. 2017, doi: 10.1109/MELE.2017.2718858.

[15] A. Barkley and E. Santi, “Online Monitoring of Network Impedances Using Digital Network Analyzer Techniques,” in 2009 Twenty-Fourth Annual IEEE Applied Power Electronics Conference and Exposition, Washington, DC, USA, Feb. 2009, pp. 440–446. doi: 10.1109/APEC.2009.4802695.

[16] H. Walker et al., “Model of Operation-and-Maintenance Costs for Photovoltaic Systems,” NREL/TP-5C00-74840, 1659995, MainId:6662, Jun. 2020. doi: 10.2172/1659995.

[17] J. Panchal, B. Wen and R. Burgos, "Power Electronics Based Self-Monitoring and Diagnosing for Photovoltaics Systems," 2021 IEEE 22nd Workshop on Control and Modelling of Power Electronics (COMPEL), Cartagena, Colombia, 2021, pp. 1-8, doi: 10.1109/COMPEL52922.2021.9646060.

[18] J. Panchal, “Power Electronics- based Photovoltaics Panel Fault Detection using Online Impedance Measurement Technique,” M.Sc. thesis, Virginia Tech, Blacksburg, VA, USA, 2022.